

# Comparative Study of Viscoelastic Arterial Wall Models in Nonlinear One-Dimensional Finite Element Simulations of Blood Flow

**Rashmi Raghu**

Department of Mechanical Engineering,  
James H. Clark Center, E3.1,  
318 Campus Drive,  
Stanford University,  
Stanford, CA 94305,  
e-mail: raghu21@stanford.edu

**Irene E. Vignon-Clementel**

INRIA Paris Rocquencourt,  
BP 105,  
78153 Le Chesnay Cedex,  
France,  
e-mail: irene.vignon-clementel@inria.fr

**C. Alberto Figueroa**

Department of Bioengineering,  
James H. Clark Center, E382,  
318 Campus Drive,  
Stanford University,  
Stanford, CA 94305,  
e-mail: cafa@stanford.edu

**Charles A. Taylor**

Department of Bioengineering,  
Department of Surgery,  
James H. Clark Center, E350B,  
318 Campus Drive,  
Stanford University,  
Stanford, CA 94305,  
e-mail: taylorca@stanford.edu

*It is well known that blood vessels exhibit viscoelastic properties, which are modeled in the literature with different mathematical forms and experimental bases. The wide range of existing viscoelastic wall models may produce significantly different blood flow, pressure, and vessel deformation solutions in cardiovascular simulations. In this paper, we present a novel comparative study of two different viscoelastic wall models in nonlinear one-dimensional (1D) simulations of blood flow. The viscoelastic models are from papers by Holenstein et al. in 1980 (model V1) and Valdez-Jasso et al. in 2009 (model V2). The static elastic or zero-frequency responses of both models are chosen to be identical. The nonlinear 1D blood flow equations incorporating wall viscoelasticity are solved using a space-time finite element method and the implementation is verified with the Method of Manufactured Solutions. Simulation results using models V1, V2 and the common static elastic model are compared in three application examples: (i) wave propagation study in an idealized vessel with reflection-free outflow boundary condition; (ii) carotid artery model with nonperiodic boundary conditions; and (iii) subject-specific abdominal aorta model under rest and simulated lower limb exercise conditions. In the wave propagation study the damping and wave speed were largest for model V2 and lowest for the elastic model. In the carotid and abdominal aorta studies the most significant differences between wall models were observed in the hysteresis (pressure-area) loops, which were larger for V2 than V1, indicating that V2 is a more dissipative model. The cross-sectional area oscillations over the cardiac cycle were smaller for the viscoelastic models compared to the elastic model. In the abdominal aorta study, differences between constitutive models were more pronounced under exercise conditions than at rest. Inlet pressure pulse for model V1 was larger than the pulse for V2 and the elastic model in the exercise case. In this paper, we have successfully implemented and verified two viscoelastic wall models in a nonlinear 1D finite element blood flow solver and analyzed differences between these models in various idealized and physiological simulations, including exercise. The computational model of blood flow presented here can be utilized in further studies of the cardiovascular system incorporating viscoelastic wall properties. [DOI: 10.1115/1.4004532]*

*Keywords:* viscoelasticity, arteries, blood flow, nonlinear one-dimensional model, finite element method, wave propagation

## 1 Introduction

Computational models of blood flow in the cardiovascular system provide insight into normal and diseased conditions in blood vessels and have applications in areas such as surgical planning and medical device design [1–6]. Methods for modeling blood flow range from zero-dimensional lumped-parameter models to one-dimensional (1D) and three-dimensional (3D) fluid–structure interaction models. Of these, lumped-parameter models do not capture wave propagation phenomena, which are of clinical importance. On the other hand, 3D methods are anatomically accurate but computationally expensive. A good compromise may be found with 1D models of blood flow that enable the study of wave propagation phenomena while being computationally inexpensive compared to 3D fluid–structure interaction models.

It is widely known that blood vessels exhibit viscoelastic properties [7–16]. However, most 1D models of blood flow, thus far,

have employed elastic constitutive behaviors [17–39]. Vessel wall viscoelasticity introduces a phase difference between pressure and wall deformation. This leads to the well-known hysteresis loop where the region within the loop is representative of the energy dissipated by the vessel wall under periodic loading. Viscoelasticity of the vessel wall is an important source of physical damping and its presence is usually attributed to smooth muscle cells [7,13,40,41]. It affects clinically relevant quantities such as flow and pressure in normal and pathological conditions. Studies have shown that viscous properties of the vessel wall are altered by hypertension [40–42], which in turn is a risk factor for atherosclerosis and aneurysm disease. For instance, viscous energy dissipation in the carotid artery was reported to be higher under hypertension conditions [41].

Numerous viscoelastic wall models derived under different experimental conditions have been proposed in the literature [9–12,14,16]. For example, Tanaka and Fung [11] derived a relationship between Lagrangian stress and stretch ratio based on relaxation tests of arterial tissue; Holenstein et al. [12] presented a relationship between pressure and cross-sectional area with parameters based on experimental data from Bergel [7] and Anliker et al. [43]; Langewouters et al. [14] presented a relationship

Contributed by the Bioengineering Division of ASME for publication in the JOURNAL OF BIOMECHANICAL ENGINEERING. Manuscript received March 10, 2011; final manuscript received June 5, 2011; published online September 6, 2011. Editor: Michael Sacks.

between pressure and cross-sectional area based on creep experiments in intact human vessels; Valdez-Jasso et al. [16] related pressure and cross-sectional area using data from in vitro physiologic loading experiments on ovine arteries. Given the wide range of experimental methods and mathematical representations, different viscoelastic wall models may produce significantly different blood flow and pressure wave solutions in cardiovascular simulations. Further, it is not straightforward to directly compare the models given the differences in their mathematical formulation and the corresponding static elastic, i.e., zero-frequency, behavior.

Previous studies on viscoelastic 1D blood flow modeling can be found in Refs. [9,12,44–52]. Segers et al. [47] compared viscoelastic models from Westerhof and Noordergraaf [9], Wesseling et al. [10], Holenstein et al. [12], and Langewouters et al. [14] in a linear 1D model of blood flow. They concluded that in peripheral vessels viscoelasticity reduced pressure pulse amplification relative to the ascending aorta. They also reported that pressure pulse in the models of Westerhof and Noordergraaf [9], Wesseling et al. [10], and Holenstein et al. [12] were within 4 mm Hg of each other at the ascending aorta and brachial and femoral arteries. Results that they obtained with the model by Langewouters et al. [14] were similar to those obtained with an elastic model. Segers et al. [47] also stated that the disparity between different viscoelastic models was limited and only the model by Langewouters et al. [14] was significantly different from the others. Studies incorporating viscoelastic wall behavior in nonlinear 1D models of blood flow can be found in Refs. [12,45,48–52]. Among these, all except Holenstein et al. [12], Reymond et al. [51], and Blanco et al. [52] employed either single vessel or single bifurcation geometric models. Holenstein et al. [12] concluded that model predictions with viscoelasticity in an idealized multibranching geometry were in better agreement with in vivo measurements than predictions without viscoelasticity. Reymond et al. [51] utilized a viscoelastic wall model based on Holenstein et al. [12] in a whole-body geometry. They reported that the effects of viscoelasticity on flow and pressure were more significant in peripheral, rather than proximal, locations. Blanco et al. [52] presented examples of coupled 3D–1D simulations with a viscoelastic wall model, but did not report any conclusions on the effects of viscoelasticity.

In this paper, we present a novel comparative study of two different viscoelastic models implemented in a nonlinear 1D finite element blood flow solver. The viscoelastic models adopted are those proposed by Holenstein et al. [12] (model V1) and Valdez-Jasso et al. [16] (model V2). The static elastic limits, or zero-frequency viscoelastic responses, for both models are chosen to be identical; thus ensuring that any differences observed between V1 and V2 in simulations are not the result of disparity in elastic components. The nonlinear 1D model of blood flow is solved using a stabilized space-time finite element method based on Refs. [23,25,53]. The finite element implementation of viscoelastic models V1 and V2 is verified using the Method of Manufactured Solutions (MMS) [54,55]. Usually, verification analyses employ the analytic solution to the linearized 1D equations of blood flow derived under the assumptions of small perturbations in nontapered vessels with spatially constant wall properties. The MMS enables the verification of a full nonlinear system of equations in tapered vessels modeled with spatially varying wall properties. The results of simulations using models V1, V2, and the static elastic model common to both, are compared in three different application examples: (i) wave propagation study in an idealized vessel with reflection-free outflow boundary condition; (ii) carotid artery model with nonperiodic boundary conditions; and (iii) subject-specific abdominal aorta model under rest and exercise conditions.

## 2 Methods

**2.1 One-Dimensional Blood Flow Equations.** The one-dimensional equations of blood flow consist of the mass conservation and momentum balance equations [53]:

$$\frac{\partial S}{\partial t} + \frac{\partial Q}{\partial z} = -\psi \quad (1)$$

$$\frac{\partial Q}{\partial t} + \frac{\partial}{\partial z} \left[ (1 + \delta) \frac{Q^2}{S} \right] + \frac{S \partial p}{\rho \partial z} = Sf + N \frac{Q}{S} + v \frac{\partial^2 Q}{\partial z^2} \quad (2)$$

The primary variables of interest are the blood flow rate  $Q$ , lumen cross-sectional area  $S$ , and blood pressure  $p$ , all of which can vary with the axial coordinate  $z$  and time  $t$ .  $\rho$  is the blood density,  $v$  is the blood kinematic viscosity, and  $N$  and  $\delta$  are based on a velocity profile function defined over the cross-section of the vessel. Here, a parabolic profile function is chosen such that  $N = -8\pi v$  and  $\delta = 1/3$ . This system requires the specification of a pressure–area relationship that describes the mechanical properties of the vessel wall. In this paper we use two different viscoelastic wall constitutive models and one elastic wall model.

**2.2 Wall Constitutive Models.** The viscoelastic models considered in this paper are those proposed by Holenstein et al. [12] (model V1) and Valdez-Jasso et al. [16] (model V2). Although both V1 and V2 relate pressure,  $p(z,t)$ , and cross-sectional area,  $S(z,t)$ , their mathematical forms are significantly different. Model V1 relates pressure  $p$  to cross-sectional area  $S$  through the instantaneous elastic response  $S^e$  such that  $S$  and  $S^e$  are related via a convolution integral. In model V2,  $p$  is related to  $S$  through a measure of strain,  $\varepsilon(z,t)$ . Here, the convolution integral relationship is defined between  $p$  and  $\varepsilon$ . The following equation provides a general representation of the two models where  $\Leftrightarrow$  indicates a convolution integral relationship and  $\leftrightarrow$  indicates a nonlinear relationship.

$$\text{Model V1: } p(z,t) \leftrightarrow S^e(z,t) \Leftrightarrow S(z,t)$$

$$\text{Model V2: } p(z,t) \Leftrightarrow \varepsilon(z,t) \leftrightarrow S(z,t) \quad (3)$$

The static elastic, i.e., zero-frequency, responses of models V1 and V2 are chosen to be identical. This common elastic model is described here followed by V1 and V2.

**2.2.1 Elastic Wall Model.** The elastic wall model characterizing the static or zero-frequency limit of models V1 and V2 is given by

$$p(z,t) = E_s(z) \frac{h(z)}{r_0(z)} \left( 1 - \left( \frac{S_0(z)}{S(z,t)} \right)^{1/2} \right) \quad (4)$$

where  $S_0(z)$  and  $r_0(z)$  are the zero-pressure area and radius, respectively,  $E_s(z)$  is the static modulus and  $h(z)$  is the wall thickness. This model is based on that proposed by Olufsen [56].

**2.2.2 Viscoelastic Model V1—Holenstein et al. (1980).** Model V1 from Holenstein et al. [12] has the following form:

$$S(z,t) = J_H(t) S^e(z,0) + \int_0^t J_H(t-\alpha) \frac{\partial S^e(z,\alpha)}{\partial \alpha} d\alpha \quad (5)$$

where  $J_H(t)$  is the normalized creep function relating  $S$  to  $S^e$ . The inverse form of Eq. (5) is

$$S^e(z,t) = E_H(t) S(z,0) + \int_0^t E_H(t-\alpha) \frac{\partial S(z,\alpha)}{\partial \alpha} d\alpha \quad (6)$$

where  $E_H(t)$  is the normalized relaxation function.  $J_H(t)$  and  $E_H(t)$  are continuous-spectrum material functions and  $J_H(t)$  is given by

$$J_H(t) = 1 + a \ln \left( \frac{\tau_{H2}}{\tau_{H1}} \right) + a \left\{ E_1 \left( \frac{t}{\tau_{H1}} \right) - E_1 \left( \frac{t}{\tau_{H2}} \right) \right\} \quad (7)$$

where  $a$  is a dimensionless constant,  $\tau_{H1}$  and  $\tau_{H2}$  are time constants such that  $\tau_{H2} > \tau_{H1}$ ,  $E_1(\cdot)$  is the exponential integral function and  $J_H(0) = 1$ . From Ref. [12] the parameter values are  $a = 0.3$ ,  $\tau_{H1} = 0.00081$  s and  $\tau_{H2} = 0.41$  s.

The convolution integrals in Eqs. (5) and (6) need to be computed using the full time history of the variables if the continuous-spectrum material functions are employed. A more computationally efficient alternative is to use a discrete-spectrum approximation to the creep and relaxation functions based on Refs. [57,58]. The approximation to  $E_H(t)$  is given by

$$E(t) = E_e + \sum_{m=1}^M E_m e^{-t/\tau_m}, \quad \text{with} \quad E_e + \sum_{m=1}^M E_m = 1 \quad (8)$$

where  $E_e$  is the normalized static modulus such that  $E_e = E_H(\infty) = 1/J_H(\infty)$ ,  $M$  is the number of discrete time constants chosen a priori,  $\tau_m$  are the time constants, and  $E_m$  are the corresponding coefficients.

At the start of the simulations the system is assumed to be in a hydrostatic state at nonzero reference pressure. The instantaneous elastic response can then be written as

$$S^e(z, t) = E_e S_{\text{ref}}(z) + \int_0^t E(t - \alpha) \frac{\partial S(z, \alpha)}{\partial \alpha} d\alpha \quad (9)$$

where  $S_{\text{ref}}$  is the area at the reference pressure. The discrete convolution implementation of this equation at time  $t + \Delta t$  is

$$S^e(z, t + \Delta t) = E_e S(z, t + \Delta t) + \sum_{m=1}^M E_m e^{-\Delta t/\tau_m} H_m(z, t) + [S(z, t + \Delta t) - S(z, t)] \sum_{m=1}^M E_m \frac{(1 - e^{-\Delta t/\tau_m})}{\Delta t/\tau_m} \quad (10)$$

where  $H_m(z, t)$  is the variable that stores the history of deformation for the  $m$ th exponential component of  $E(t)$  and is updated for each time step as follows:

$$H_m(z, t) = e^{-\Delta t/\tau_m} H_m(z, t - \Delta t) + [S(z, t) - S(z, t - \Delta t)] \frac{(1 - e^{-\Delta t/\tau_m})}{\Delta t/\tau_m} \quad (11)$$

The instantaneous elastic response  $S^e$  is then related to pressure  $p$  by the expression:

$$p(z, t) = E_s(z) \frac{h(z)}{r_0(z)} \left( 1 - \left( \frac{S_0^e(z)}{S^e(z, t)} \right)^{1/2} \right) \quad (12)$$

where  $S_0^e(z) = E_e S_0(z)$ . If all the  $E_m$  parameters in the relaxation function are zero then  $S^e(z, t) = E_e S(z, t)$  and substituting this into Eq. (12) gives the elastic relationship in Eq. (4).

**Table 1 Parameters of the normalized relaxation function for Model V1 given in Eq. (8) with  $M=8$  and  $E_e=3.49 \times 10^{-1}$**

Relaxation function parameters for Model V1	
$E_m$	$\tau_m$ (s)
$1.47 \times 10^{-1}$	$7.16 \times 10^{-4}$
$2.08 \times 10^{-1}$	$1.50 \times 10^{-3}$
$7.62 \times 10^{-2}$	$4.21 \times 10^{-3}$
$8.13 \times 10^{-2}$	$9.92 \times 10^{-3}$
$4.81 \times 10^{-2}$	$2.55 \times 10^{-2}$
$4.34 \times 10^{-2}$	$6.20 \times 10^{-2}$
$3.59 \times 10^{-2}$	$1.52 \times 10^{-1}$
$1.08 \times 10^{-2}$	$3.96 \times 10^{-1}$

2.2.3 *Viscoelastic Model V2—Valdez-Jasso et al. (2009)*. Model V2 from Valdez-Jasso et al. [16] relates strain  $\varepsilon$  and pressure  $p$  as follows:

$$\varepsilon(t) = \varepsilon(0) e^{-t/\tau_\varepsilon} + \frac{r_0}{E_s h \tau_\varepsilon} \left( \tau_\sigma p(t) - \tau_\sigma p(0) e^{-t/\tau_\varepsilon} + \frac{\tau_\varepsilon - \tau_\sigma}{\tau_\varepsilon} \int_0^t e^{-(t-\alpha)/\tau_\varepsilon} p(\alpha) d\alpha \right) \quad (13)$$

where the strain  $\varepsilon$  and the cross-sectional area  $S$  are related by

$$\varepsilon(t) = 1 - \left( \frac{S_0}{S(t)} \right)^{1/2} \quad (14)$$

Here,  $S_0$  and  $r_0$  are the area and radius at zero pressure, respectively,  $h$  is the thickness of the wall,  $\tau_\sigma$  and  $\tau_\varepsilon$  are time constants. In general, all parameters and variables in Eqs. (13) and (14) are allowed to vary with respect to the axial coordinate  $z$ .

At the start of the simulations the system is considered to be in a hydrostatic state and pressure  $p$  can then be written as a function of strain  $\varepsilon$  as follows:

$$p(z, t) = \frac{h(z)}{r_0(z)} \left( E_s(z) \varepsilon_{\text{ref}}(z) + \int_0^t E(z, t - \alpha) \frac{\partial \varepsilon(z, \alpha)}{\partial \alpha} d\alpha \right) \quad (15)$$

where  $\varepsilon_{\text{ref}}$  is the strain at the non-zero reference pressure such that  $\varepsilon_{\text{ref}}(z) = 1 - (S_0(z)/S_{\text{ref}}(z))^{1/2}$ ,  $S_{\text{ref}}$  is the area at reference pressure,  $E_s(z)$  is the static elastic (zero-frequency) wall modulus, and  $E(z, t)$  is the relaxation function given by

$$E(z, t) = E_s(z) + E_1(z) e^{-t/\tau_\sigma(z)} \quad (16)$$

where  $E_1(z) = E_s(z) ((\tau_\varepsilon(z)/\tau_\sigma(z)) - 1)$ .

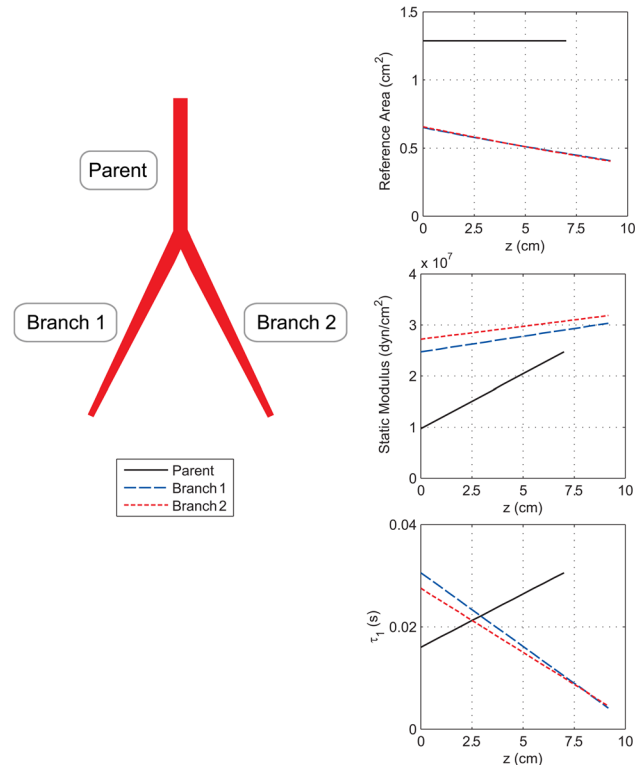


**Fig. 1 Bifurcation model for MMS verification. Variations of reference area, static modulus, and time constant ( $\tau_1$ ) are shown along each vessel segment for viscoelastic model V2.**

The discrete convolution implementation of Eq. (15) is

$$p(z, t + \Delta t) = \frac{h(z)}{r_0(z)} \left\{ E_s(z) \varepsilon(z, t + \Delta t) + E_1(z) e^{-\Delta t / \tau_\sigma(z)} H_1(z, t) + [\varepsilon(z, t + \Delta t) - \varepsilon(z, t)] E_1(z) \frac{(1 - e^{-\Delta t / \tau_\sigma(z)})}{\Delta t / \tau_\sigma(z)} \right\} \quad (17)$$

where  $H_1(z, t)$  is the history variable and is updated for each time step as

$$H_1(z, t) = e^{-\Delta t / \tau_\sigma(z)} H_1(z, t - \Delta t) + [\varepsilon(z, t) - \varepsilon(z, t - \Delta t)] E_1(z) \frac{(1 - e^{-\Delta t / \tau_\sigma(z)})}{\Delta t / \tau_\sigma(z)} \quad (18)$$

In Eq. (16) if  $\tau_\sigma = \tau_\varepsilon$  then model V2 reduces to the elastic relationship in Eq. (4).

**2.3 Finite Element Method.** A space-time finite element discontinuous Galerkin method is used to solve the nonlinear 1D blood flow equations. The method presented here extends the

work by Wan et al. [25] and Vignon and Taylor [23] to account for viscoelastic wall models. We rewrite Eqs. (1) and (2) in a quasi-linear conservative form:

$$\frac{\partial \mathbf{U}}{\partial t} + \frac{\partial \mathbf{F}(\mathbf{U})}{\partial z} - \mathbf{K} \frac{\partial^2 \mathbf{U}}{\partial z^2} = \mathbf{G}(\mathbf{U}) \quad (19)$$

with

$$\mathbf{U} = \begin{Bmatrix} U_1 \\ U_2 \end{Bmatrix} = \begin{Bmatrix} S \\ Q \end{Bmatrix} \quad \mathbf{K} = \begin{bmatrix} 0 & 0 \\ 0 & v \end{bmatrix}$$

$$\mathbf{F}(\mathbf{U}) = \begin{Bmatrix} Q \\ (1 + \delta) \frac{Q^2}{S} + \frac{1}{\rho} A_F(z, t) \end{Bmatrix} \quad (20)$$

$$\mathbf{G}(\mathbf{U}) = \begin{Bmatrix} -\psi \\ Sf + N \frac{Q}{S} + \frac{1}{\rho} C_F(z, t) \end{Bmatrix}$$

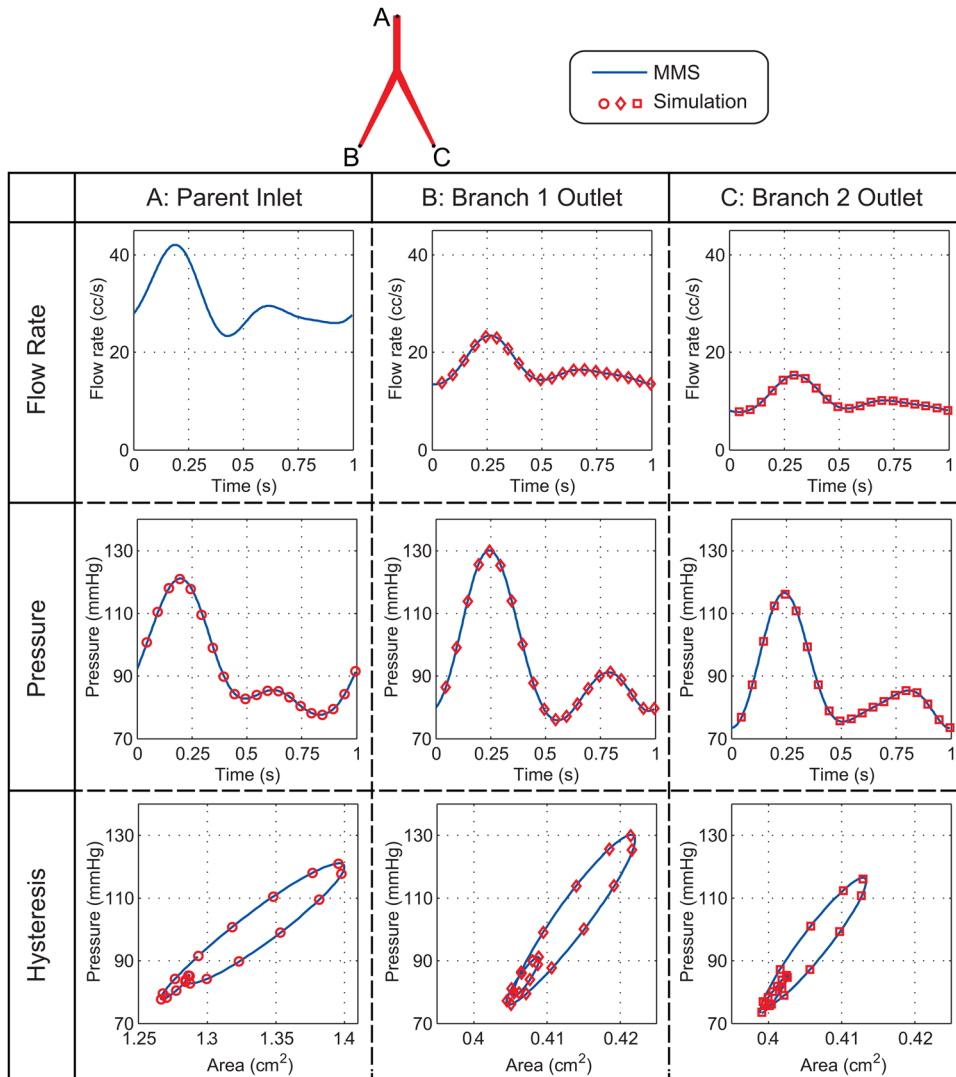


**Fig. 2** MMS verification results for the finite element implementation of model V2. The MMS flow rate at the inlet is prescribed as a boundary condition for the simulations.

Here,  $A_F(z, t)$  and  $C_F(z, t)$  are given by

$$\begin{aligned} A_F(z, t) &= \int_0^t S(z, \alpha) \frac{\partial p(z, \alpha)}{\partial \alpha} d\alpha \\ C_F(z, t) &= \int_0^t \frac{\partial S(z, \alpha)}{\partial z} \frac{\partial p(z, \alpha)}{\partial \alpha} - \frac{\partial p(z, \alpha)}{\partial z} \frac{\partial S(z, \alpha)}{\partial \alpha} d\alpha \end{aligned} \quad (21)$$

The weak formulation of the initial boundary value problem is defined as follows: In a domain  $\Omega = [0, L]$ , find  $\mathbf{U}$  in  $V = \{V : \Omega \times ]0, T[ \Rightarrow \mathbb{R}^2 | V(z, t) \in H_0^1(\Omega \times ]0, T[)\}$  such that  $\forall \mathbf{W} = [W_1 \ W_2]^T \in V$ :

$$\begin{aligned} &\int_0^T \int_0^L \left( -\mathbf{W}_{,t}^T \mathbf{U} - \mathbf{W}_{,z}^T \mathbf{F}(\mathbf{U}) + \mathbf{W}_{,z}^T \mathbf{K} \mathbf{U}_{,z} - \mathbf{W}^T \mathbf{G}(\mathbf{U}) \right) dz dt \\ &+ \int_0^L \mathbf{W}^T(z, T) \mathbf{U}(z, T) dz - \int_0^L \mathbf{W}^T(z, 0) \mathbf{U}^0(z) dz \\ &- \int_0^T [\mathbf{W}^T(\mathbf{F}(\mathbf{U}) - \mathbf{K} \mathbf{U}_{,z})]_{z=0} dt + \int_0^T [\mathbf{W}^T(\mathbf{F}(\mathbf{U}) - \mathbf{K} \mathbf{U}_{,z})]_{z=L} dt = 0 \end{aligned} \quad (22)$$

where  $\mathbf{U}^0(z) = [Q^0(z), \ S^0(z)]^T$  are prescribed initial conditions. Here, we usually prescribe a flow rate at the inlet of the domain through a Dirichlet boundary condition. At the outlets, the domain is coupled to the rest of the circulation through operators  $\mathbf{M}$  and  $\mathbf{H}$  such that  $[\mathbf{F}(\mathbf{U}) - \mathbf{K} \mathbf{U}_{,z}]_{z=L} = [\mathbf{M}(\mathbf{U}) + \mathbf{H}]_{z=L}$ . These operators usually correspond to a resistance, impedance or Resistance-Capacitance-Resistance (RCR, Windkessel) boundary condition. Details of this can be found in Ref. [23].

Using a piecewise-constant approximation in time and a piecewise-linear approximation in space for  $\mathbf{U}$  and  $\mathbf{W}$ , the residual

for the nonlinear system of equations over each time slab can be written as

$$\begin{aligned} \mathfrak{R}_A^{n+1}(\mathbf{U}^{n+1}) &= \Delta t_n \left\{ \int_0^L (-N_{A,z} \mathbf{F}^{n+1}(\mathbf{U}^{n+1}) + N_{A,z} \mathbf{K} N_{B,z} \mathbf{U}_B^{n+1}) dz \right. \\ &+ \int_0^L (-N_A \mathbf{G}^{n+1}(\mathbf{U}^{n+1})) dz - [N_A(\mathbf{F}^{n+1}(\mathbf{U}^{n+1}) \\ &- \mathbf{K} N_{B,z} \mathbf{U}_B^{n+1})]_{z=0} + [N_A(\mathbf{M}^{n+1}(\mathbf{U}^{n+1}) \\ &+ \mathbf{H}^{n+1})]_{z=L} \left. \right\} + \int_0^L N_A (N_B \mathbf{U}_B^{n+1} - N_B \mathbf{U}_B^n) dz \\ &+ \Delta t_n \sum_e \int_{\Omega_e} \left\{ (\mathbf{A}_S^{n+1}(\mathbf{U}^{n+1}))^T N_{A,z} \right. \\ &- \mathbf{C}_S^{n+1}(\mathbf{U}^{n+1})^T N_A \tau^{n+1}(\mathbf{U}^{n+1}) \\ &\times (\mathbf{A}_S^{n+1}(\mathbf{U}^{n+1}) N_{B,z} \mathbf{U}_B^{n+1} - \mathbf{C}_S^{n+1}(\mathbf{U}^{n+1}) \\ &\times N_B \mathbf{U}_B^{n+1}) \left. \right\} dz = 0 \end{aligned} \quad (23)$$

for  $A = 1, 2, \dots, N_{\text{nodes}}$ , where  $N_A(z)$  and  $N_B(z)$  are the piecewise-linear shape functions and  $\Delta t_n$  is the time step size. For the sake of simplifying notation the dependence of  $\mathbf{F}^{n+1}$  and  $\mathbf{G}^{n+1}$  on the history of  $\mathbf{U}$  due to the viscoelastic wall models is not explicitly represented in the equation.  $\tau(\mathbf{U})$  in Eq. (23) is a matrix of stabilization parameters based on Wan et al. [25] and the terms  $\mathbf{A}_S(\mathbf{U})$  and  $\mathbf{C}_S(\mathbf{U})$  are

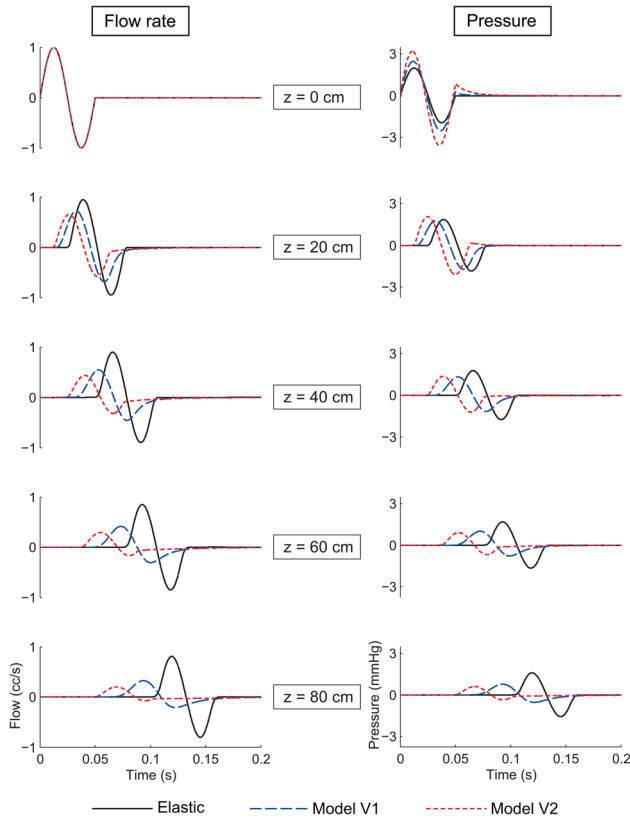


**Fig. 3** Wave propagation study showing flow and pressure waves at different locations in the vessel for viscoelastic models V1, V2, and the elastic wall model. The vessel is 80 cm long with reflection-free (characteristic impedance) boundary condition at the outlet.

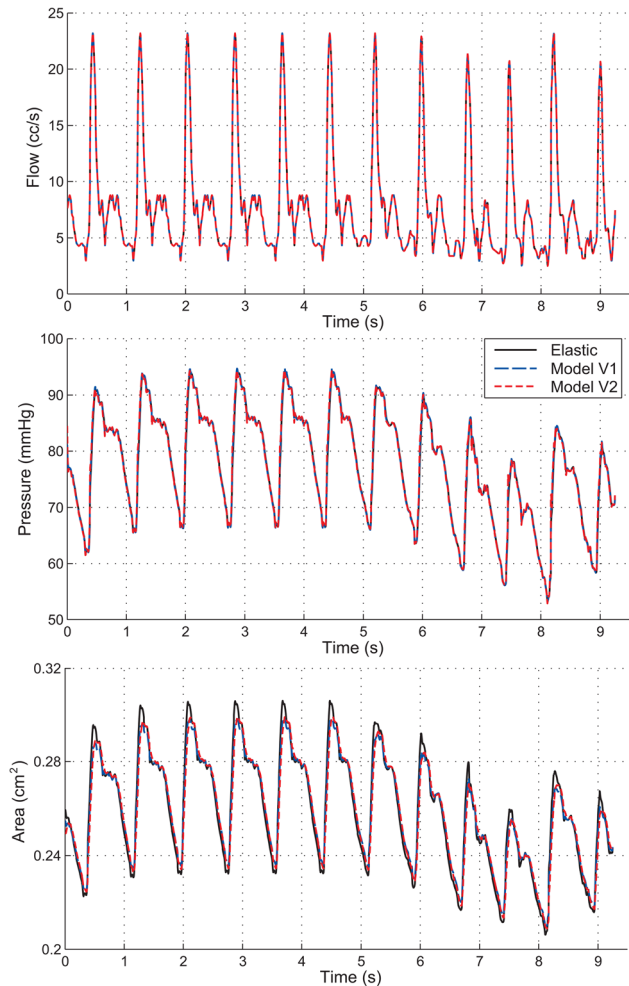


**Fig. 4** Carotid artery model with transient in-flow boundary condition and RCR boundary condition at the outlet. Flow (prescribed), pressure, and cross-sectional area are shown for the inlet of the model.

$$\mathbf{A}_S(\mathbf{U}) = \begin{bmatrix} 0 & 1 \\ -(1+\delta)\frac{\rho^2}{S^2} + \frac{\delta}{\rho}\frac{\partial p}{\partial S} & 2(1+\delta)\frac{\rho}{S} \end{bmatrix}, \quad (24)$$

$$\mathbf{C}_S(\mathbf{U}) = \begin{bmatrix} \frac{-\psi}{S} & 0 \\ f - \frac{1}{\rho}\left(\frac{\partial p}{\partial z} - \frac{\partial p}{\partial S}\frac{\partial S}{\partial z}\right) & \frac{N}{S} \end{bmatrix}$$

At a bifurcation point pressure continuity and conservation of mass are enforced through Lagrange multipliers as shown in Ref. [25]. A Newton–Raphson technique is used to solve nonlinear system of equations (23) assuming that  $\partial\tau/\partial\mathbf{U}^{n+1} = 0$  for the tangent matrix computation.

**2.4 Method of Manufactured Solutions.** The MMS enables comprehensive verification of systems involving the solution of partial differential equations (PDEs) [54,55]. In the case of the nonlinear 1D equations of blood flow the MMS allows verification utilizing general tapered vessel geometries and spatially varying wall properties, exercising all the nonlinear terms in the governing equations. This type of verification cannot be achieved using the analytic solutions to the linearized 1D equations of blood flow as these are limited to non-tapered vessel geometries with spatially constant wall properties under small-perturbations conditions.

The MMS verification strategy starts with the manufacturing of analytic expressions or “solutions” to the governing PDEs. The

manufactured solutions need not satisfy the governing equations exactly, need not be physically realistic but need to be differentiable and result in nontrivial expressions for all terms present in the PDEs. The manufactured solutions, when substituted in the governing equations, result in non-zero remainder terms that can be added as source terms to the original PDEs. The manufactured solutions are also used to generate the appropriate boundary conditions for the problem. Subsequently, the governing equations with source terms and boundary conditions are solved by the numerical method. The resulting numerical solutions are compared to the manufactured solutions in order to verify the numerical method. More details can be found in Refs. [54,55,59].

### 3 Results

In this section, we first present the verification of the finite element implementation of model V2 using the MMS procedure. The verification of model V1 is not presented here for the sake of brevity. We then compare the different constitutive models in the following application examples: (i) wave propagation study in an idealized vessel with reflection-free outflow boundary condition; (ii) carotid artery model with nonperiodic boundary conditions; and (iii) subject-specific abdominal aorta model under rest and exercise conditions. For all simulations the time constants for the relaxation function of model V1 are given in Table 1. The density and dynamic viscosity of blood are set to 1.06 g/cm<sup>3</sup> and 0.04 g/(cm s), respectively.

**3.1 Verification With the Method of Manufactured Solutions.** The idealized bifurcation geometry used in the verification of model V2 is depicted in Fig. 1, showing the spatial variations in the reference cross-sectional area, static elastic modulus, and the time constant of relaxation for each vessel segment in the bifurcation. Periodic expressions for flow rate and strain are

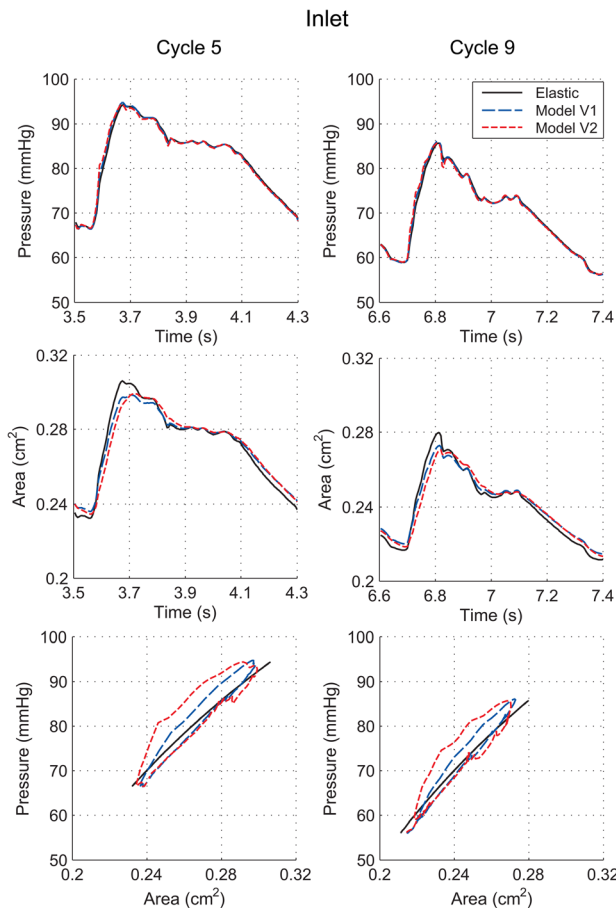


**Fig. 5** Inlet pressure, cross-sectional area and hysteresis for the carotid artery model corresponding to the fifth and ninth cardiac cycles in Fig. 4

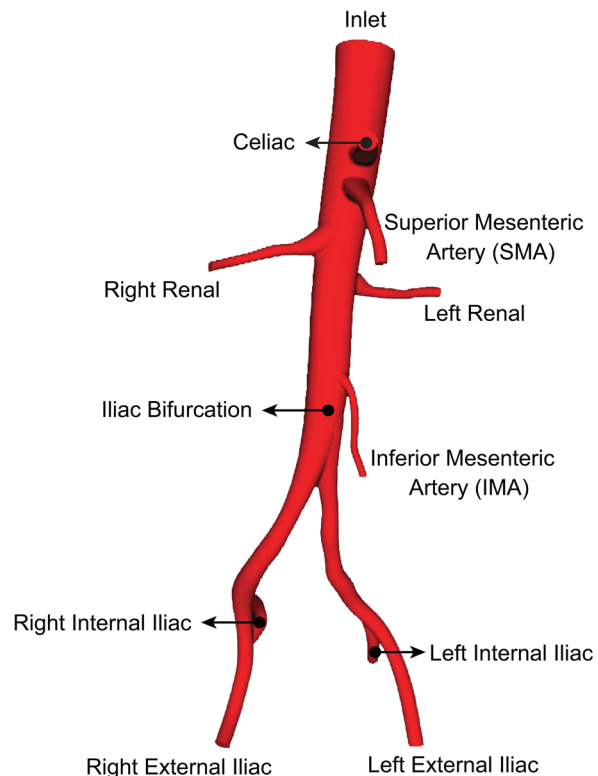


**Fig. 6** Abdominal aorta geometry of a normal subject from Yeung et al. [61]

manufactured first, followed by cross-sectional area and pressure manufactured from strain via Eqs. (14) and (17). The manufactured flow rate and time-varying resistance are prescribed as inflow and outflow boundary conditions, respectively. The finite element mesh consists of 54 elements and the time step size is  $5 \times 10^{-3}$  s

Figure 2 shows the manufactured and numerical solutions for flow rate, pressure, and hysteresis (pressure–area) loops. The hysteresis loop is traversed in a clockwise manner over time. The numerical solutions match the manufactured solutions closely. The root-mean-square (rms) values of the percentage error of the nu-

merical solution with respect to the manufactured solution are 0.10%, 0.15%, and 0.018% for flow rate, pressure, and area, respectively. Furthermore, we observed monotonous decrease of the error upon decreasing the mesh and time step sizes.

**3.2 Wave Propagation Study in an Idealized Vessel With Reflection-Free Outflow Boundary Condition.** In this study, we consider a vessel of length 80 cm with a reference radius of 0.31 cm. A transient, small amplitude flow pulse is prescribed at the inlet and a reflection-free boundary condition is prescribed at

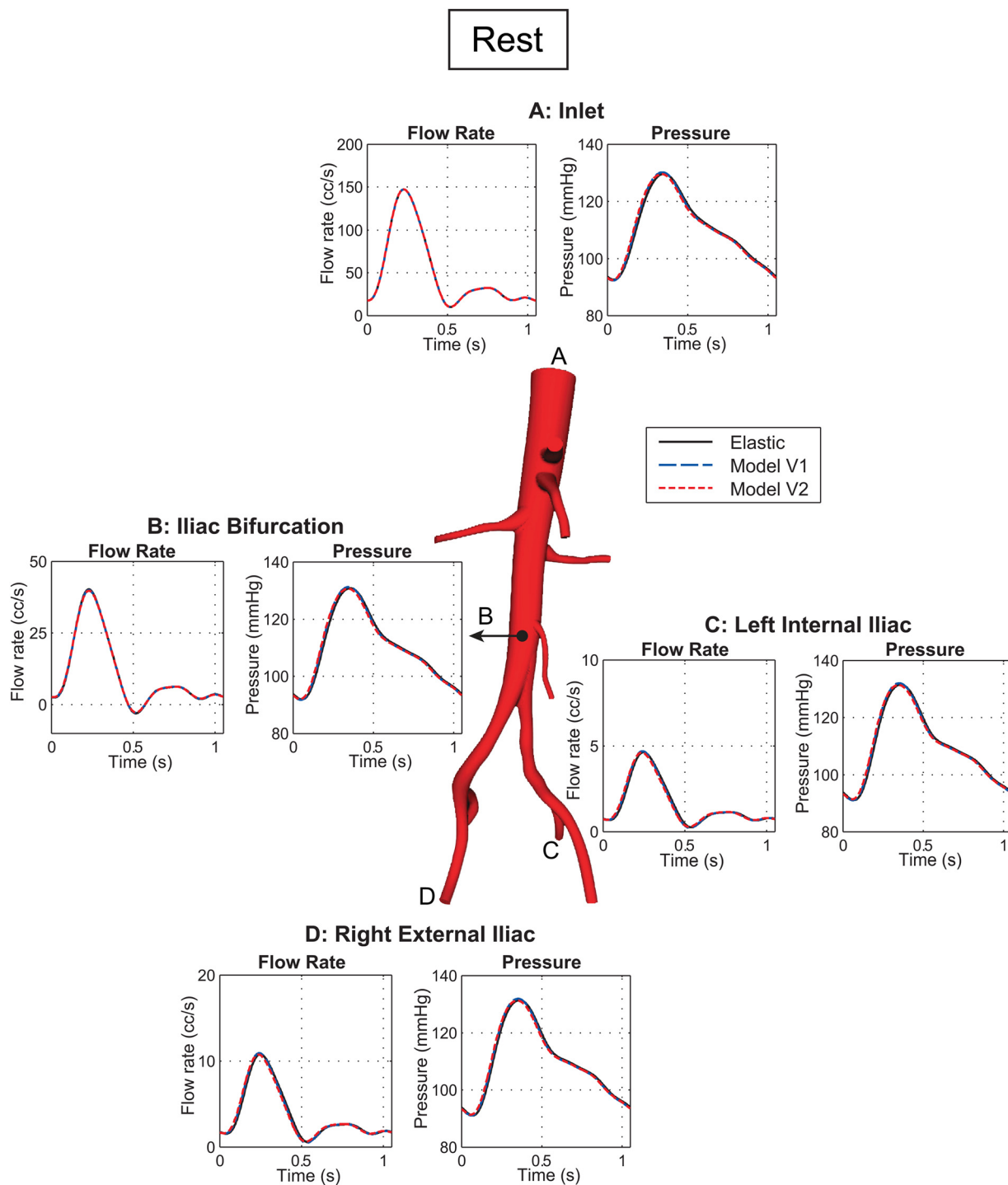


**Fig. 7** Flow rate and pressure under resting conditions at the inlet, iliac bifurcation, left internal iliac, and right external iliac artery outlets for the subject-specific abdominal aorta model

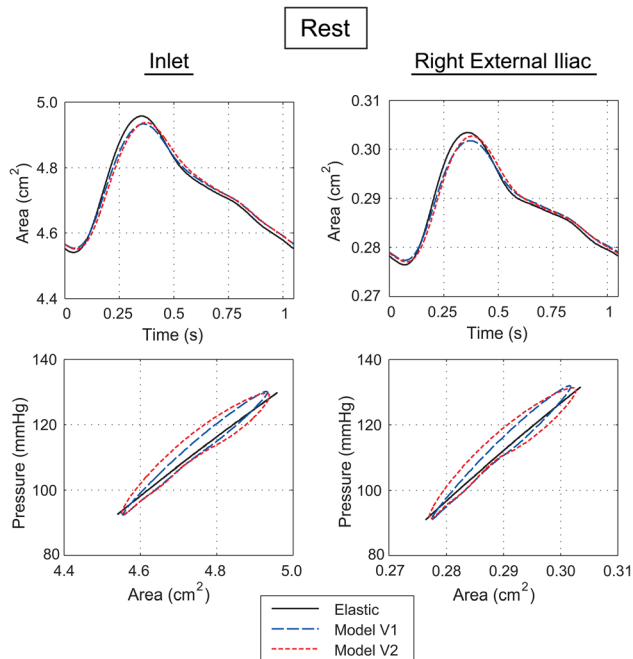


**Fig. 8 Cross-sectional area and hysteresis under resting conditions at the inlet and right external iliac outlet of the subject-specific abdominal aorta model**

the outlet via a characteristic impedance spectrum. This allows the study of wave propagation without reflections in the system. The static elastic modulus of V1, V2 and the elastic models is set to  $1.26 \times 10^7$  dyn/cm<sup>2</sup>, such that the elastic wave speed is 745 cm/s and within the physiologic range. The time constant for model V2 is set to  $9 \times 10^{-3}$  s, which is the value for the carotid artery in Ref. [16]. The vessel is discretized into 1280 elements and the time step size chosen for simulations is  $1 \times 10^{-4}$  s.

Figure 3 shows the flow and pressure waves at different longitudinal locations. There are noticeable differences in the amplitudes of the flow and pressure waves for the different constitutive models. The largest damping and wave speed correspond to model V2. On the other hand, as expected, the lowest damping and wave speed are observed for the elastic wall model. For models V1 and V2, we can also observe an exponential decay in the pressure waveforms at the inlet starting at approximately 0.05 s. This is due to the relaxation phenomenon associated with viscoelastic materials.

**3.3 Carotid Artery Model With Nonperiodic Boundary Conditions.** In this study, we investigate the effects of viscoelastic wall models in conjunction with physiologically realistic, nonperiodic boundary conditions in a common carotid artery model. The length of the vessel is 3.5 cm and the reference radius is 0.28 cm. A nonperiodic flow boundary condition is prescribed at the inlet and an RCR (Windkessel) boundary condition at the outlet. The static elastic modulus of V1, V2 and the elastic model is set to  $4.18 \times 10^6$  dyn/cm<sup>2</sup>. The vessel geometry, boundary conditions, and static elastic modulus are those used by Vignon-Clementel et al. in Ref. [60]. The inflow exhibits cycle-to-cycle variations over eight cardiac cycles as measured by ultrasound. The time constant for model V2 is set to  $9 \times 10^{-3}$  s. A spatial discretization consisting of 35 elements and a time step size of  $5 \times 10^{-3}$  s is utilized for all simulations.

Figure 4 shows the inlet flow rate, pressure, and cross-sectional area for the three different wall models. We initiated the analysis by prescribing five periodic cycles to ensure that a physiologic periodic state was reached before the transient part of the simula-

tions (cycles 6–12). Here, no significant differences are observed in pressure waveforms between the material models. The rms differences in inlet pressure for V1 and V2 relative to the elastic model over all cardiac cycles are less than 1 mm Hg. On the other hand, differences are seen in the cross-sectional area with smaller amplitude oscillations for V1 and V2 compared to the elastic model. Figure 5 shows inlet pressure, area, and hysteresis for the fifth and ninth cycles of the simulations. In both cycles, the difference in pressure pulse between the viscoelastic and elastic models is less than 3%. However, the amplitude of cross-sectional area oscillations for the viscoelastic models is up to 16% smaller compared to the elastic model. Both V1 and V2 show hysteresis as observed in the pressure–area plots. Model V2 shows the most dissipative behavior, with a hysteresis loop area twice as large as that of model V1. Hysteresis curves are also steeper for the viscoelastic models indicating stiffer effective behavior than the elastic model.

**3.4 Subject-Specific Abdominal Aorta Model Under Rest and Exercise Conditions** In this study, we consider the 1D model representing a subject-specific abdominal aorta from Yeung et al. (2006) [61] (see Fig. 6) under rest and simulated lower limb exercise conditions for the three constitutive models. Rest and simulated exercise inflow waveforms and outflow RCR parameters are chosen following the methodology presented by Les et al. (2010) [62]. Relative to resting conditions, the simulated exercise heart rate and average inflow are increased by 52% and 93%, respectively. Each outflow RCR boundary condition consists of a proximal resistance in series with a parallel combination of a capacitance and distal resistance. The distal resistance values of the lower limb RCR outlet boundary conditions are decreased to simulate exercise, whereas the distal resistances of the remaining branches are increased. The static elastic modulus,  $E_s$ , of all material models is derived from the following expression based on Olufsen [56]:

$$E_s(z) \frac{h(z)}{r_{\text{ref}}(z)} = \frac{1}{(1 - \vartheta^2)} \left( k_1 e^{k_2 r_{\text{ref}}(z)} + k_3 \right). \quad (25)$$

where  $k_1 = 2 \times 10^7$  dyn/cm<sup>2</sup>,  $k_2 = -22.53$  cm<sup>-1</sup>,  $k_3 = 8.65 \times 10^5$  dyn/cm<sup>2</sup>,  $\vartheta = 0.5$  is the Poisson's ratio for the wall,  $r_{\text{ref}}$  is the reference radius of the vessel, and  $h$  is the wall thickness. Values for  $h$  are obtained from the ratio of thickness to zero-pressure radius in Ref. [16]. The time-constant ( $\tau_\sigma$ ) values for model V2 are spatially varying based on data in Ref. [16]. At the inlet  $\tau_\sigma = 1.6 \times 10^{-2}$  s,  $\tau_\sigma = 3.06 \times 10^{-2}$  s at the celiac outlet and iliac bifurcation, and  $\tau_\sigma = 4.1 \times 10^{-3}$  s at all other outlets. A spatial discretization consisting of 820 elements is utilized for all simulations. Time step sizes of  $3 \times 10^{-3}$  s and  $2 \times 10^{-3}$  s are used for the rest and exercise simulations, respectively.

Figure 7 shows flow rate and pressure under rest conditions at the inlet, iliac bifurcation, left internal iliac, and right external iliac outlets. Here, no significant differences are observed in flow rate and pressure between the material models. The differences in flow amplitude and pressure pulse for V1 and V2 relative to the elastic model are less than 4% at any spatial location. The inlet pressure pulse is 38 mm Hg for V1 and 37 mm Hg for V2 and the elastic model. At the outlets of the iliac arteries amplification of pressure pulse relative to the inlet is lower for the viscoelastic models. Segers et al. [47] reported the same trend for the femoral artery relative to the ascending aorta. Figure 8 shows cross-sectional area and hysteresis loops under resting conditions for the inlet and right external iliac outlet. At these locations, the amplitude of cross-sectional area oscillations for the viscoelastic models is up to 10% lower than for the elastic case. The hysteresis loop for V2 is at least 73% larger than V1, showing that V2 has a more dissipative behavior. Hysteresis loops are also steeper for V1 and V2, indicating a stiffer effective behavior relative to the elastic model.

Figure 9 shows flow rate and pressure under exercise conditions at the inlet, iliac bifurcation, left internal iliac, and right external iliac outlets. Here, we observe a positive phase shift of flow and pressure waves for V1 and V2 relative to the elastic model with pressure showing the larger phase difference. The phase lag between flow and pressure at the inlet is smaller for the visco-elastic models. The differences in flow amplitude and pressure pulse for V1 and V2 are less than 7% relative to the elastic model at any spatial location. The inlet pressure pulses are 68 mm Hg, 65 mm Hg, and 64 mm Hg for V1, V2, and the elastic model,

respectively. Figure 10 shows cross-sectional area and hysteresis plots under exercise conditions for the inlet and right external iliac outlet. Here, the amplitude of area oscillations is up to 9% lower for V1 and V2 relative to the elastic model. The hysteresis loop for model V2 is at least 79% larger than V1.

Results also show that differences in flow and pressure between material models are more pronounced under exercise than rest. For instance, rms differences in pressure between V1 and the elastic model over the entire geometry for one cycle are 0.8 mm Hg and 3.9 mm Hg under rest and exercise conditions, respectively.

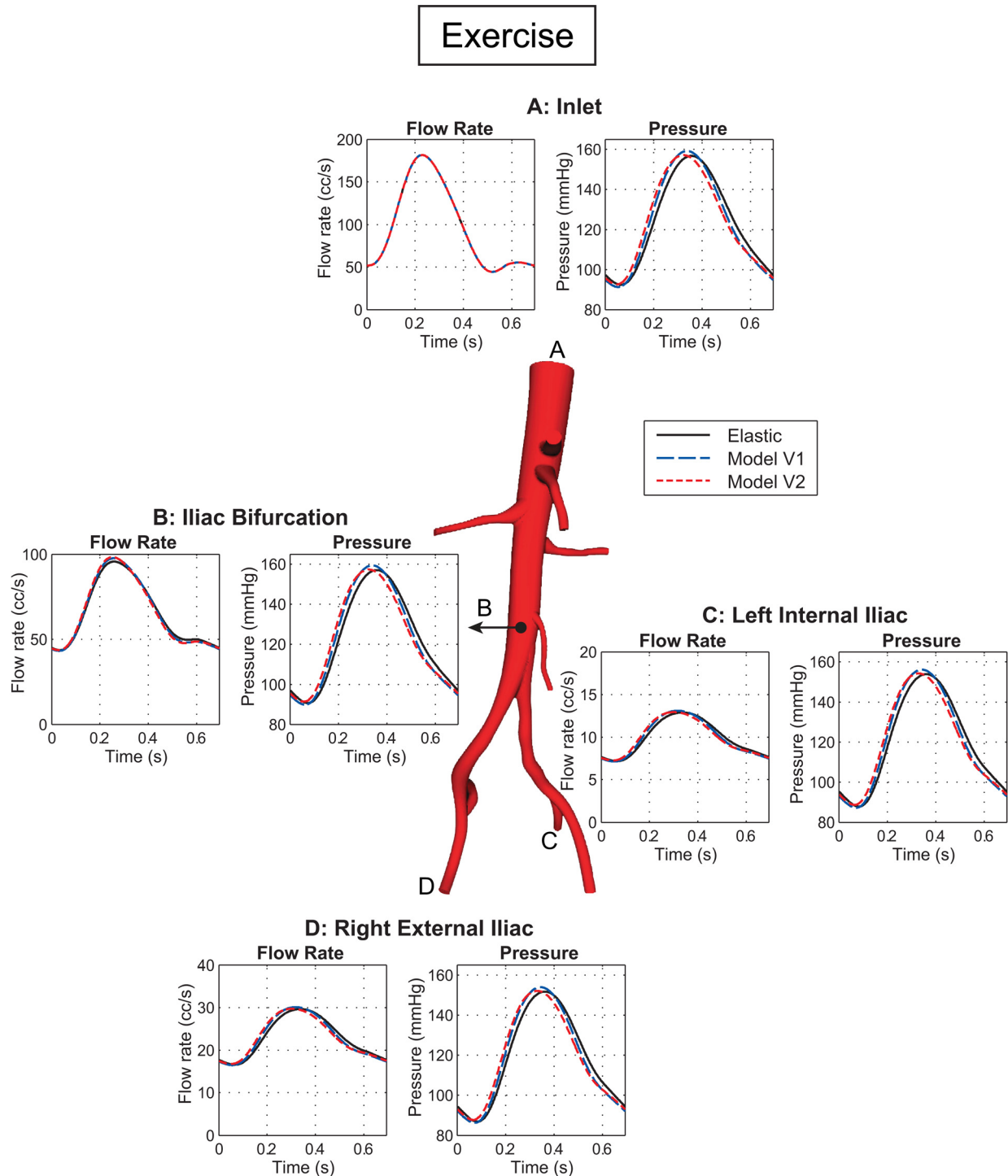
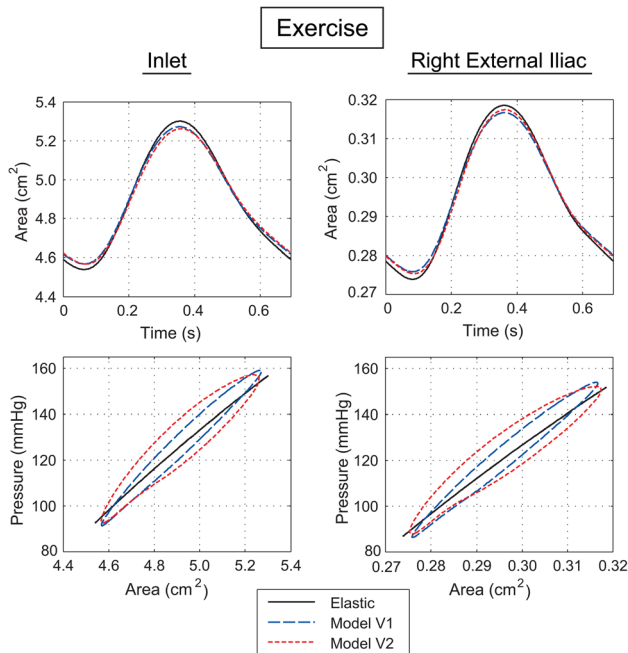


Fig. 9 Flow rate and pressure under lower limb exercise conditions at the inlet, iliac bifurcation, left internal iliac, and right external iliac artery outlets for the subject-specific abdominal aorta model



**Fig. 10 Cross-sectional area and hysteresis under lower limb exercise conditions at the inlet and right external iliac outlet of the subject-specific abdominal aorta model**

Between V2 and the elastic model the rms differences in pressure are 1.2 mm Hg and 5.9 mm Hg under rest and exercise, respectively. Inlet pressure pulse differences between the material models are larger in the exercise condition. The ratio of hysteresis loop size for model V2 relative to V1 is also higher under exercise at the inlet and at all outlets.

#### 4 Discussion and Future Work

Numerous models representing the viscoelastic behavior of arterial walls can be found in the literature [9–12,14,16]. These models have different mathematical forms and experimental bases, making it difficult to perform direct comparisons. In this paper, we presented the first comparative studies of viscoelastic wall models in nonlinear 1D simulations of blood flow. The viscoelastic models chosen for this work are those from Holenstein et al. [12] (model V1) and Valdez-Jasso et al. [16] (model V2). A common static elastic component was utilized in both models.

We first presented the implementation of V1 and V2 in a nonlinear 1D finite element blood flow solver. This implementation was verified using the Method of Manufactured Solutions in a bifurcation model with tapered vessels and spatially varying wall properties. The MMS procedure is a more comprehensive verification method than verifications using the analytic solution to the linearized 1D equations of blood flow derived under the assumptions of small perturbations in non-tapered vessels with spatially constant wall properties.

We compared V1, V2 and elastic models in three different application examples. First, we presented a wave propagation study in an idealized vessel with reflection-free outflow boundary condition. In this study, damping and speed of flow and pressure waves were largest for model V2 and lowest for the elastic model. Second, we studied a carotid artery model with nonperiodic boundary conditions. Here, significant differences between viscoelastic and elastic models were observed in a cross-sectional area and hysteresis at the inlet. The final study was a subject-specific abdominal aorta model under rest and exercise conditions. Differences in flow and pressure between material models were not noticeably significant under resting conditions. On the other hand, phase differences were observed for pressure under exercise con-

ditions and the inlet pressure pulse for V1 was larger than the pulse for V2 and the elastic model. To the best of our knowledge, this study is the first to compare the impact of different viscoelastic wall models under exercise conditions.

Combined observations from the carotid and abdominal aorta studies showed the following: The most significant differences between models were observed in the hysteresis loops, which were larger for model V2 than V1, indicating that V2 is a more dissipative model. Hysteresis loops were also steeper for both viscoelastic models thus showing stiffer effective behavior relative to the elastic model. The cross-sectional area oscillations over the cardiac cycle were smaller for the viscoelastic models. The impact of wall models on pressure was noticeably significant only in the abdominal aorta study under exercise conditions. On the other hand, the impact of wall models on flow rate was not significant as flow is determined primarily by mass conservation and the prescribed Dirichlet inflow condition.

The nonlinear 1D finite element model of blood flow presented in this paper can be useful to analyze the sensitivity of flow, pressure, and hysteresis to uncertainty in viscoelastic model parameters. One limitation of 1D models of blood flow is that they do not capture complex 3D flow patterns, which may be significant in exercise conditions and in the presence of structures such as stenoses. Wall viscoelasticity must be incorporated in a 3D fluid-structure interaction (FSI) model of blood flow in order to investigate its impact in the presence of complex flow.

Viscoelasticity of the vessel wall is usually attributed to smooth muscle cells [7,13,40,41], which are present in higher proportion in peripheral vessels [7,63]. Therefore, viscoelasticity of downstream vessels needs to be considered when prescribing outflow boundary conditions in blood flow simulations. The nonlinear 1D blood flow model presented in this paper can be coupled to 3D FSI models to provide outflow boundary conditions that incorporate downstream wall viscoelasticity. This would provide a comprehensive model of blood flow to analyze the impact of wall viscoelasticity in coupled 3D and 1D domains.

#### Acknowledgment

R.R. was supported by the Stanford Graduate Fellowship and the Benchmark Capital Congenital Cardiovascular Fellowship. This work was also supported by the INRIA international associated-team funding. The authors would like to thank Dr. Hyun-Jin Kim and Dr. Andrea Les for providing information relevant to the abdominal aorta study.

#### References

- [1] Anor, T., Grinberg, L., Baek, H., Madsen, J. R., Jayaraman, M. V., and Karniadakis, G. E., 2010, "Modeling of Blood Flow in Arterial Trees," Wiley Interdiscip. Rev.: Syst. Biol. Med., 2(5), pp. 612–623.
- [2] Taylor, C. A., and Steinman, D. A., 2010, "Image-Based Modeling of Blood Flow and Vessel Wall Dynamics: Applications, Methods and Future Directions: Sixth International Bio-Fluid Mechanics Symposium and Workshop, March 28–30, (2008) Pasadena, California," Ann. Biomed. Eng., 38(3), pp. 1188–1203.
- [3] Quarteroni, A., Tuveri, M., and Veneziani, A., 2000, "Computational Vascular Fluid Dynamics: Problems, Models and Methods," Comput. Visualiz. Sci., 2, pp. 163–197.
- [4] Taylor, C. A., and Draney, M. T., 2004, "Experimental and Computational Methods in Cardiovascular Fluid Mechanics," Annu. Rev. Fluid Mech., 36(1), pp. 197–231.
- [5] Vignon-Clementel, I. E., Marsden, A. L., and Feinstein, J. A., 2010, "A Primer on Computational Simulation in Congenital Heart Disease for the Clinician," Progr. Pediatr. Cardiol., 30(1–2), pp. 3–13.
- [6] Migliavacca, F., and Dubini, G., 2005, "Computational Modeling of Vascular Anastomoses," Biomech. Model. Mechanobiol., 3(4), pp. 235–250.
- [7] Bergel, D. H., 1961, "The Dynamic Elastic Properties of the Arterial Wall," J. Physiol., 156(3), pp. 458–469.
- [8] Learoyd, B. M., and Taylor, M. G., 1966, "Alterations With Age in the Viscoelastic Properties of Human Arterial Walls," Circ. Res., 18, pp. 278–292.
- [9] Westerhof, N., and Noordergraaf, A., 1970, "Arterial Viscoelasticity: A Generalized Model: Effect on Input Impedance and Wave Travel in the Systematic Tree," J. Biomech., 3, pp. 357–379.
- [10] Wesseling, K. H., Weber, H., and de Wit, B., 1973, "Estimated Five Component Viscoelastic Model Parameters for Human Arterial Walls," J. Biomech., 6, pp. 13–24.

- [11] Tanaka, T. T., and Fung, Y. C., 1974, "Elastic and Inelastic Properties of the Canine Aorta and Their Variation Along the Aortic Tree," *J. Biomech.*, **7**(4), pp. 357–370.
- [12] Holenstein, R., Niederer, P., and Anliker, M., 1980, "A Viscoelastic Model for Use in Predicting Arterial Pulse Waves," *J. Biomech. Eng.*, **102**(4), pp. 318–325.
- [13] Cox, R. H., 1984, "Viscoelastic Properties of Canine Pulmonary Arteries," *Am. J. Physiol. Heart Circ. Physiol.*, **246**(1), pp. H90–H96.
- [14] Langewouters, G. J., Wesseling, K. H., and Goedhard, W. J. A., 1985, "The Pressure Dependent Dynamic Elasticity of 35 Thoracic and 16 Abdominal Human Aortas in Vitro Described by a Five Component Model," *J. Biomech.*, **18**(8), pp. 613–620.
- [15] Imura, T., Yamamoto, K., Satoh, T., Kanamori, K., Mikami, T., and Yasuda, H., 1990, "In Vivo Viscoelastic Behavior in the Human Aorta," *Circ. Res.*, **66**(5), pp. 1413–1419.
- [16] Valdez-Jasso, D., Haider, M. A., Banks, H. T., Santana, D. B., Germán, Y. Z., Armentano, R. L., and Olufsen, M. S., 2009, "Analysis of Viscoelastic Wall Properties in Ovine Arteries," *IEEE Trans. Biomed. Eng.*, **56**(2), pp. 210–219.
- [17] Alastruey, J., Parker, K. H., Peiró, J., Byrd, S. M., and Sherwin, S. J., 2007, "Modelling the Circle of Willis to Assess the Effects of Anatomical Variations and Occlusions on Cerebral Flows," *J. Biomech.*, **40**(8), pp. 1794–1805.
- [18] Azer, K., and Peskin, C. S., 2007, "A One-Dimensional Model of Blood Flow in Arteries with Friction and Convection Based on the Womersley Velocity Profile," *Cardiovasc. Eng.*, **7**(2), pp. 51–73.
- [19] Bessems, D., Rutten, M., and Van De Vosse, F., 2007, "A Wave Propagation Model of Blood Flow in Large Vessels Using an Approximate Velocity Profile Function," *J. Fluid Mech.*, **580**, pp. 145–168.
- [20] Huo, Y., and Kassab, G. S., 2007, "A Hybrid One-Dimensional/Womersley Model of Pulsatile Blood Flow in the Entire Coronary Arterial Tree," *Am. J. Physiol. Heart Circ. Physiol.*, **292**(6), pp. H2623–H2633.
- [21] Steele, B. N., Olufsen, M. S., and Taylor, C. A., 2007, "Fractal Network Model for Simulating Abdominal and Lower Extremity Blood Flow During Resting and Exercise Conditions," *Computer Methods in Biomechanics and Biomedical Engineering*, **10**(1), pp. 39–51.
- [22] Formaggia, L., Lamponi, D., Tuveri, M., and Veneziani, A., 2006, "Numerical Modeling of 1D Arterial Networks Coupled With a Lumped Parameters Description of the Heart," *Comput. Methods Biomech. Biomed. Eng.*, **9**(5), pp. 273–288.
- [23] Vignon, I. E., and Taylor, C. A., 2004, "Outflow Boundary Conditions for One-Dimensional Finite Element Modeling of Blood Flow and Pressure Waves in Arteries," *Wave Motion*, **39**, pp. 361–374.
- [24] Sherwin, S. J., Franke, V., Peiró, J., and Parker, K., 2003, "One-Dimensional Modelling of a Vascular Network in Space-Time Variables," *J. Eng. Math.*, **47**, pp. 217–250.
- [25] Wan, J., Steele, B., Spicer, S. A., Strohsband, S., Feijóo, G. R., Hughes, T. J. R., and Taylor, C. A., 2002, "A One-Dimensional Finite Element Method for Simulation-Based Medical Planning for Cardiovascular Disease," *Comput. Methods Biomech. Biomed. Eng.*, **5**(3), pp. 195–206.
- [26] Smith, N. P., Pullan, A. J., and Hunter, P. J., 2001, "An Anatomically Based Model of Transient Coronary Blood Flow in the Heart," *SIAM J. Appl. Math.*, **62**(3), pp. 990–1018.
- [27] Olufsen, M. S., Peskin, C. S., Kim, W. Y., Pedersen, E. M., Nadim, A., and Larsen, J., 2000, "Numerical Simulation and Experimental Validation of Blood Flow in Arteries With Structured-Tree Outflow Conditions," *Ann. Biomed. Eng.*, **28**, pp. 1281–1299.
- [28] Stergiopoulos, N., Young, D. F., and Rogge, T. R., 1992, "Computer Simulation of Arterial Flow With Applications to Arterial and Aortic Stenoses," *J. Biomech.*, **25**(12), pp. 1477–1488.
- [29] Papanayotou, C. J., Cherruault, Y., and de La Rochefoucauld, B., 1990, "A Mathematical Model of the Circle of Willis in the Presence of an Arteriovenous Anomaly," *Comput. Math. Appl.*, **20**(4–6), pp. 199–206.
- [30] Hillen, B., Hoogstraten, H. W., and Post, L., 1986, "A Mathematical Model of the Flow in the Circle of Willis," *J. Biomech.*, **19**(3), pp. 187–194.
- [31] Zagzoule, M., and Marc-Vergnes, J.-P., 1986, "A Global Mathematical Model of the Cerebral Circulation in Man," *J. Biomech.*, **19**(12), pp. 1015–1022.
- [32] Kufahl, R. H., and Clark, M. E., 1985, "A Circle of Willis Simulation Using Distensible Vessels and Pulsatile Flow," *J. Biomech. Eng.*, **107**(2), pp. 112–122.
- [33] Stettler, J. C., Niederer, P., and Anliker, M., 1981, "Theoretical Analysis of Arterial Hemodynamics Including the Influence of Bifurcations Part I: Mathematical Model and Prediction of Normal Pulse Patterns," *Ann. Biomed. Eng.*, **9**, pp. 145–164.
- [34] Stettler, J. C., Niederer, P., Anliker, M., and Casty, M., 1981, "Theoretical Analysis of Arterial Hemodynamics Including the Influence of Bifurcations Part II: Critical Evaluation of Theoretical Model and Comparison with Noninvasive Measurements of Flow Patterns in Normal and Pathological Cases," *Ann. Biomed. Eng.*, **9**, pp. 165–175.
- [35] Raines, J. K., Jaffrin, M. Y., and Shapiro, A. H., 1974, "A Computer Simulation of Arterial Dynamics in the Human Leg," *J. Biomech.*, **7**, pp. 77–91.
- [36] Schaaf, B. W., and Abbrecht, P. H., 1972, "Digital Computer Simulation of Human Systemic Arterial Pulse Wave Transmission: A Nonlinear Model," *J. Biomech.*, **5**(4), pp. 345–364.
- [37] Wemple, R. R., and Mockros, L. F., 1972, "Pressure and Flow in the Systemic Arterial System," *J. Biomech.*, **5**, pp. 629–641.
- [38] Westerhof, N., Bosman, F., De Vries, C. J., and Noordergraaf, A., 1969, "Analog Studies of the Human Systemic Arterial Tree," *J. Biomech.*, **2**(2), pp. 121–143.
- [39] Noordergraaf, A., Verdouw, P. D., and Boom, H. B. K., 1963, "The Use of an Analog Computer in a Circulation Model," *Progr. Cardiovasc. Dis.*, **5**(5), pp. 419–439.
- [40] Simon, A., and Levenson, J., 2001, "Effect of Hypertension on Viscoelasticity of Large Arteries in Humans," *Curr. Hypertens. Rep.*, **3**(1), pp. 74–79.
- [41] Armentano, R. L., Barra, J. G., Santana, D. B., Pessana, F. M., Graf, S., Craiem, D., Brandani, L. M., Baglivo, H. P., and Sanchez, R. A., 2006, "Smart Damping Modulation of Carotid Wall Energetics in Human Hypertension: Effects of Angiotensin-Converting Enzyme Inhibition," *Hypertension*, **47**(3), pp. 384–390.
- [42] Armentano, R., Megnien, J. L., Simon, A., Bellenfant, F., Barra, J., and Levenson, J., 1995, "Effects of Hypertension on Viscoelasticity of Carotid and Femoral Arteries in Humans," *Hypertension*, **26**, pp. 48–54.
- [43] Anliker, M., Histan, M. B., and Ogden, E., 1968, "Dispersion and Attenuation of Small Artificial Pressure Waves in the Canine Aorta," *Circ. Res.*, **23**(4), pp. 539–551.
- [44] Avolio, A. P., 1980, "Multi-Branched Model of the Human Arterial System," *Med. Biol. Eng. Comput.*, **18**(6), pp. 709–718.
- [45] Reuderink, P. J., Hoogstraten, H. W., Sijkema, P., Hillen, B., and Westerhof, N., 1989, "Linear and Nonlinear One-Dimensional Models of Pulse Wave Transmission at High Womersley Numbers," *J. Biomech.*, **22**(8/9), pp. 819–827.
- [46] Fitchett, D. H., 1991, "LV-Arterial Coupling: Interactive Model to Predict Effect of Wave Reflections on LV Energetics," *Am. J. Physiol. Heart Circ. Physiol.*, **261**, pp. H1026–H1033.
- [47] Segers, P., Stergiopoulos, N., Verdonck, P., and Verhoeven, R., 1997, "Assessment of Distributed Arterial Network Models," *Med. Biol. Eng. Comput.*, **35**(6), pp. 729–736.
- [48] Pontrelli, G., 2002, "A Mathematical Model of Flow in a Liquid-Filled Visco-Elastic Tube," *Med. Biol. Eng. Comput.*, **40**(5), pp. 550–556.
- [49] Formaggia, L., Lamponi, D., and Quarteroni, A., 2003, "One-Dimensional Models for Blood Flow in Arteries," *J. Eng. Math.*, **47**(3), pp. 251–276.
- [50] Bessems, D., Giannopapa, C. G., Rutten, M. C. M., and van de Vosse, F. N., 2008, "Experimental Validation of a Time-Domain-Based Wave Propagation Model of Blood Flow in Viscoelastic Vessels," *J. Biomech.*, **41**, pp. 284–291.
- [51] Raymond, P., Merenda, F., Perren, F., Rüfenacht, D., and Stergiopoulos, N., 2009, "Validation of a One-Dimensional Model of the Systemic Arterial Tree," *Am. J. Physiol. Heart Circ. Physiol.*, **297**, pp. H208–H222.
- [52] Blanco, P. J., Urquiza, S. A., and Feijóo, R. A., 2010, "Assessing the Influence of Heart Rate in Local Hemodynamics Through Coupled 3D–1D–0D Models," *Int. J. Numer. Methods Biomed. Eng.*, **26**(April), pp. 890–903.
- [53] Hughes, T. J. R., and Lubliner, J., 1973, "On the One-Dimensional Theory of Blood Flow in the Larger Vessels," *Math. Biosci.*, **18**(1–2), pp. 161–170.
- [54] Roache P. J., 2002, "Code Verification by the Method of Manufactured Solutions," *J. Fluids Eng.*, **124**, pp. 4–10.
- [55] Knupp, P., and Salari K., 2002, *Verification of Computer Codes in Computational Science and Engineering*, Chapman & Hall/CRC, Boca Raton, FL.
- [56] Olufsen, M. S., 1999, "Structured Tree Outflow Condition for Blood Flow in Larger Systemic Arteries," *Am. J. Physiol. Heart Circ. Physiol.*, **276**, pp. 257–268.
- [57] Puso, M. A., and Weiss, J. A., 1998, "Finite Element Implementation of Anisotropic Quasi-Linear Viscoelasticity Using a Discrete Spectrum Approximation," *J. Biomech. Eng.*, **120**(1), pp. 62–70.
- [58] Holzapfel, G. A., Gasser, T. C., and Stadler, M., 2002, "A Structural Model for the Viscoelastic Behavior of Arterial Walls: Continuum Formulation and Finite Element Analysis," *Eur. J. Mech. A/Solids*, **21**, pp. 441–463.
- [59] Raghu, R., and Taylor, C. A., 2011, "Verification of a One-Dimensional Finite Element Method for Modeling Blood Flow in the Cardiovascular System Incorporating a Viscoelastic Wall Model," *Finite Elem. Anal. Design*, **47**(6), pp. 586–592.
- [60] Vignon-Clementel, I. E., Figueroa, C. A., Jansen, K. E., and Taylor, C. A., 2010, "Outflow Boundary Conditions for 3D Simulations of Non-Periodic Blood Flow and Pressure Fields in Deformable Arteries," *Comput. Methods Biomech. Biomed. Eng.*, **13**(5), pp. 625–640.
- [61] Yeung, J. J., Kim, H. J., Abbruzzese, T. A., Vignon-Clementel, I. E., Draney-Blomme, M. T., Yeung, K. K., Perkash, I., Herfkens, R. J., Taylor, C. A., and Dalman R. L., 2006, "Aortoiliac Hemodynamic and Morphologic Adaptation to Chronic Spinal Cord Injury," *J. Vasc. Surg.*, **44**(6), pp. 1254–1265.e1.
- [62] Les, A. S., Shadden, S. C., Figueroa, C. A., Park, J. M., Tedesco, M. M., Herfkens, R. J., Dalman, R. L., and Taylor C. A., 2010, "Quantification of Hemodynamics in Abdominal Aortic Aneurysms During Rest and Exercise Using Magnetic Resonance Imaging and Computational Fluid Dynamics," *Ann. Biomed. Eng.*, **38**(4), pp. 1288–1313.
- [63] Milnor, W. R., 1989, *Hemodynamics*, Williams & Wilkins, Baltimore, MD.